Article

Site Identity and Importance in Cosubstituted Bixbyite In$_2$O$_3$

Karl Rickert [1], Jeremy Harris [1], Nazmi Sedefoglu [2], Hamide Kavak [3], Donald E. Ellis [4] and Kenneth R. Poeppelmeier [1,*]

[1] Department of Chemistry, Northwestern University, Evanston, IL 60208, USA; karlrickert2011@u.northwestern.edu (K.R.); jeremyharris2013@u.northwestern.edu (J.H.)
[2] Department of Physics, Osmaniye Korkut Ata University, Osmaniye 80000, Turkey; nazmisedefoglu@gmail.com
[3] Physics Department, Cukurova University, Adana 01330, Turkey; hkavak@cu.edu.tr
[4] Department of Physics and Astronomy, Northwestern University, Evanston, IL 60208, USA; don-ellis@northwestern.edu
[*] Correspondence: krp@northwestern.edu; Tel.: +1-847-491-3505

Abstract: The bixbyite structure of In$_2$O$_3$ has two nonequivalent, 6-coordinate cation sites and, when Sn is doped into In$_2$O$_3$, the Sn prefers the "*b*-site" and produces a highly conductive material. When divalent/tetravalent cation pairs are cosubstituted into In$_2$O$_3$, however, the conductivity increases to a lesser extent and the site occupancy is less understood. We examine the site occupancy in the Mg$_x$In$_{2-2x}$Sn$_x$O$_3$ and Zn$_x$In$_{2-2x}$Sn$_x$O$_3$ systems with high resolution X-ray and neutron diffraction and density functional theory computations, respectively. In these sample cases and those that are previously reported in the M$_x$In$_{2-2x}$Sn$_x$O$_3$ (M = Cu, Ni, or Zn) systems, the solubility limit is greater than 25%, ensuring that the *b*-site cannot be the exclusively preferred site as it is in Sn:In$_2$O$_3$. Prior to this saturation point, we report that the M^{2+} cation always has at least a partial occupancy on the *d*-site and the Sn^{4+} cation has at least a partial occupancy on the *b*-site. The energies of formation for these configurations are highly favored, and prefer that the divalent and tetravalent substitutes are adjacent in the crystal lattice, which suggests short range ordering. Diffuse reflectance and 4-point probe measurements of Mg$_x$In$_{2-x}$Sn$_x$O$_3$ demonstrate that it can maintain an optical band gap >2.8 eV while surpassing 1000 S/cm in conductivity. Understanding how multiple constituents occupy the two nonequivalent cation sites can provide information on how to optimize cosubstituted systems to increase Sn solubility while maintaining its dopant nature, achieving maximum conductivity.

Keywords: bixbyite; indium oxide; transparent conducting oxide

1. Introduction

Bixbyite indium oxide is the basis of industrially important n-type transparent conducting oxides, which are in turn fundamental components of flat panel displays, touch screens, and solar cells [1–3]. Specifically, tin-doped indium oxide (ITO) is a highly effective transparent conducting oxide that derives its desirable conductivity from the formation of Frank-Köstlin clusters [4]. The concentration of these clusters are directly influenced by the solubility of tin in the bixbyite lattice. As higher conductivities are being demanded of transparent conductors, increasing the solubility of tin in the bixbyite structure is of interest.

One proven method to increase the solubility of tin in In$_2$O$_3$ is to perform a cosubstitution of M^{2+} and Sn^{4+} into In$_2$O$_3$, where M = Mg, Ca, Ni, Cu, Zn, or Cd, to form M$_x$In$_{2-2x}$Sn$_x$O$_3$ which maintains the bixbyite structure of In$_2$O$_3$. In so doing, solubility limits as high as *x* = 0.5 can be achieved, which

is approximately double the amount of tin in ITO [5,6]. This does not double the conductivity of ITO, however, as the cosubstitution is not true doping because the tetravalent tin is counterbalanced by a divalent cation when replacing two trivalent cations. A complete counterbalancing effect would substantially decrease the conductivity when compared to ITO, but in some cases an inherent off stoichiometry in the divalent and tetravalent cation is observed, which results in a dopant effect and high conductivity [7].

In ITO, the dopant favors one of the two nonequivalent cation sites present in the bixbyite structure. Both sites are 6-coordinate and can be described as a cube with two anion positions vacant along either a body diagonal (*b*-site) or a face diagonal (*d*-site). Computational and experimental studies agree that the tin in ITO favors the *b*-site [8–10]. The *b*-site comprises 25% of the cation sites in the bixbyite structure, shown in Figure 1, which would inherently limit the solubility of tin, but the solubility limit is actually lower, resulting in mixed indium and tin occupancy of the *b*-site. The solubility limits of cosubstituted bixbyite, however, can occupy up to 50% of the cation sites and therefore must alter the *d*-site either exclusively or in combination with the *b*-site. The impact of multiple constituents (i.e., only Sn vs. M/Sn pairs) on the electronic properties has already drawn investigative interest, particularly for M = Zn, but the importance of site occupancy has not yet been tied to either the multiple constituents or the electronic properties [11,12]. The constituent identities and their site preferences have been linked to crystal structure, however, as exhibited by the cosubstitution of Zn/Ge pairs. In this instance, the system forms a single defined phase instead of a solid solution and departs from the bixbyite structure in order to provide a 4-coordinate site for Ge [13].
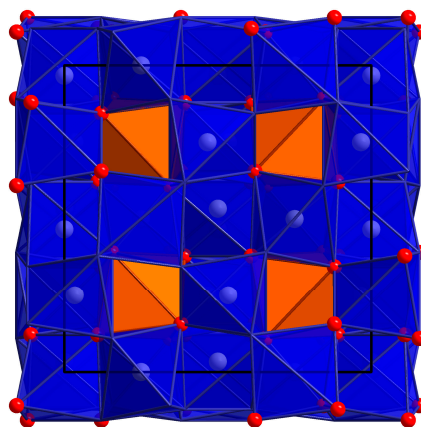

Figure 1. The unit cell (black lines) of bixbyite In_2O_3 as viewed along the *b* axis, showing the locations of the *b*-sites (opaque, orange, 25% of cation sites) and the *d*-sites (transparent, blue, 75%).

A thorough understanding of how multiple constituents occupy the two nonequivalent cation sites in bixbyite can provide information on how to optimize the cosubstituted systems to increase tin solubility while maintaining its dopant nature. Herein, the cosubstituted bixbyite system $M_xIn_{2-2x}Sn_xO_3$, with M = Mg or Zn, is evaluated and the site occupancies and electronic properties are compared to each other and reported cosubstituted systems. The $Zn_xIn_{2-2x}Sn_xO_3$ system (commonly referred to as either ZITO or IZTO) is widely studied as a transparent conductor and the electronic properties have been previously reported, but here it is investigated with a computational approach that examines local site structure [6,11,14–19]. $Mg_xIn_{2-2x}Sn_xO_3$, in contrast, has been the subject of a single bulk study and a thin film study and here is the subject of a more thorough structural and property study [5,20]. Local coordination environments and site occupancies are difficult to confidently determine with experimental techniques, which average sites in a bulk sample, and thus computational approaches are more informative in these approaches. Both methods are presented here and suggest that the *b*-site is still the more important site for the tetravalent cation and thus the conductivity of these materials.

2. Results

2.1. Solid Solution Characterization

The lattice parameters for as-synthesized $Mg_xIn_{2-2x} - Sn_xO_3$ ($x \leq 0.3$) are determined by X-ray diffraction (XRD) and the lattice parameters for $Zn_xIn_{2-2x} - Sn_xO_3$ ($x \leq 0.5$) are calculated via density functional theory (DFT). Both sets of lattice parameters are provided in Figure S1 and the XRD patterns used to calculate the parameters for $Mg_xIn_{2-2x} - Sn_xO_3$ are shown in Figure S2. The lattice parameters exhibit linear decreases, following Vegard's Law, as a result of the smaller radii of Mg/Sn (0.72 Å/0.69 Å) and Zn/Sn (0.74 Å/0.69 Å) pairs compared to that of In/In (0.80 Å) pairs [21–23]. The $Mg_xIn_{2-2x} - Sn_xO_3$ lattice parameters closely match those that have been previously reported for the system, but the $Zn_xIn_{2-2x} - Sn_xO_3$ lattice parameters are systematically expanded, a somewhat common occurrence when DFT results are compared with experimental results [24,25]. The solubility limit of the Mg/Sn pairing (0.3) is slightly higher than previous reports (0.25) [5]. Surpassing the solubility limit in $Mg_xIn_{2-2x} - Sn_xO_3$ produces the easily identified SnO_2 and MgO phases. Off stoichiometry trials (i.e., where [Mg] $\neq$ [Sn]) were attempted, but were unsuccessful in creating the Sn rich phases reported via thin film synthesis [20].

2.2. $Mg_{0.1}In_{1.8}Sn_{0.1}O_3$ Structural Refinement

A joint Rietveld refinement of synchrotron XRD and time-of-flight neutron diffraction (TOF-ND) data for $Mg_{0.1}In_{1.8}Sn_{0.1}O_3$ ($x = 0.1$) is considered. The overall bixbyite structure is maintained and the goodness-of-fit parameters for a joint Rietveld refinement of each probable occupancy pattern are provided in Table 1. The Rietveld refinement and difference patterns are provided in Figure S3. As can be observed, all of the occupancy patterns display similar fits, with differences in total R_{wp} values being less than 0.0012. The χ^2 and Bragg factors also display similar values. One factor that negatively impacts the goodness of fit parameters for the XRD refinement is a systematic, asymmetric peak shape with tails at lower d values. Such a shape is typically associated with stacking or deformation faults. The fits discussed here do not account for this asymmetry, as the exact cause is unclear and thus an appropriate model cannot be applied. Even without accounting for this asymmetry, the fits are reasonable but maintain residual intensity on each reflection. Using Hamilton's R test with 45 refined parameters, 545 XRD reflections, and 1080 ND reflections, the difference between the R_{wp} values ≥ 0.2208 and the R_{wp} values ≤ 0.2199 is statistically significant at the 0.5% level. That is, the hypothesis that the fits without Mg on the d-site are correct is rejected [26]. The differences between the remaining models, however, are not statistically significant. The qualitative assessment of the difference patterns for these fits do not offer assistance in selecting a site. These data suggest that a "correct" structural model must contain Mg on the d-site, but the exact quantity is unknown and the Sn location is inconclusive. It is possible that this ambiguity arises from the aforementioned asymmetric peak shapes that are not accounted for in the refinement, but it is also possible that introducing a model to handle the asymmetry would decrease the ability to accurately discern occupancies, maintaining the inconclusive results.

Table 1. Goodness of fit parameters for joint X-ray diffraction (XRD) and ND Rietveld refinement of $Mg_{0.1}In_{1.8}Sn_{0.1}O_3$ with different cation occupancies. Indium occupies the remaining site percentages.

Mg Location (%)		Sn Location (%)		R_{wp}			$\chi2$	R_{F^2}	
b-site	d-site	b-site	d-site	Total	XRD	ND		XRD	ND
20	0	0	6.67	0.2209	0.2694	0.0423	24.32	0.0947	0.1442
0	6.67	20	0	0.2198	0.2680	0.0426	24.09	0.0917	0.1528
20	0	20	0	0.2208	0.2692	0.0433	24.30	0.0940	0.1420
0	6.67	0	6.67	0.2198	0.2679	0.0431	24.08	0.0913	0.1544
10	3.33	10	3.33	0.2199	0.2681	0.0420	24.09	0.0898	0.1482

2.3. $Zn_xIn_{2-2x}Sn_xO_3$ Formation Energy Computations

The formation energies of $Zn_xIn_{2-2x}Sn_xO_3$ for different values of x are calculated and provided in Figure 2a. As the amount of substitutes increases, the favorability of the reaction decreases and the results are prone to a higher variability. Even with this increased variability, the data set displays a good linear fit for $x > 0$ until the final data point ($x = 0.50$) which changes the R^2 value from 0.9817 to 0.9515. Note that previous reports place the experimentally determined solubility limit as $x \leq 0.4$ in $Zn_xIn_{2-2x}Sn_xO_3$ [6]. The higher variability is a result of the greater possible variety of site occupancies of the substitutes that are considered. These different occupancies are considered in Figure 2b for a single Zn/Sn pair. A shorter Zn-Sn separation difference is the most favored configuration, regardless as to the specific site occupancies. The relative favorability between the different site occupancies is maintained with distance and the overall most favorable occupancy pattern is Zn present on the *d*-site, Sn present on the *b*-site, and the Zn and Sn present in neighboring positions.
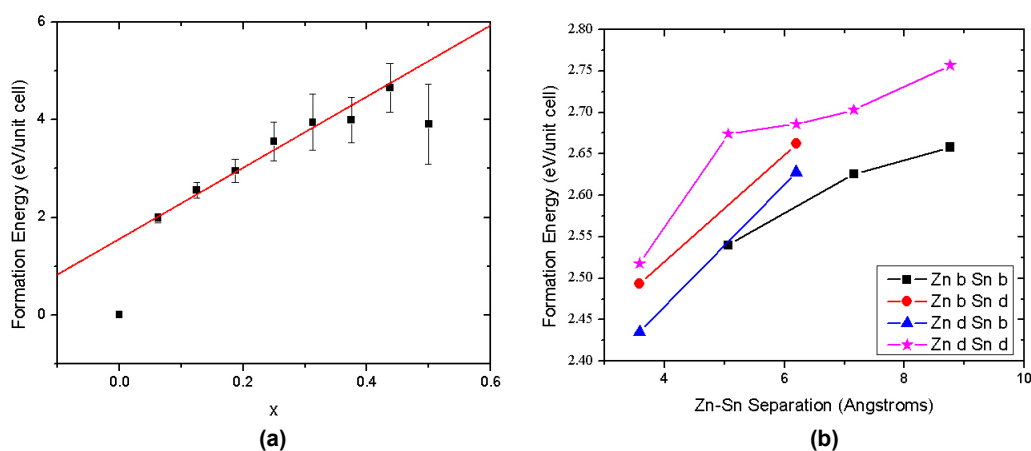

Figure 2. Formation energies as a function of (**a**) cosubstitution amounts of $Zn_xIn_{2-2x}Sn_xO_3$ and (**b**) Zn-Sn separation for different site occupancies (i.e., "Zn b Sn b" represents Zn and Sn present on the b site). The linear fit in (**a**) is for $0 < x < 0.5$. All values in (**a**,**b**) are normalized to the -449.832 eV of In_2O_3 ($x = 0$), thus the greater values have less favored formation energies.

2.4. $Mg_xIn_{2-2x}Sn_xO_3$ Conductivity and Band Gap Measurements

The original discovery of the $Mg_xIn_{2-2x}Sn_xO_3$ solid solution assessed the optical properties of $x = 0.05$ and 0.25 and the temperature-dependent conductivity of $x = 0.05$. From this preliminary characterization, the band gap is known to be similar to that of ITO, but the conductivity is approximately one order of magnitude lower than that of ITO [5]. The Seebeck coefficients of the as-synthesized materials (see Figure S4) have a negative parity, identifying the $Mg_xIn_{2-2x}Sn_xO_3$ system as n-type. In the original investigation, the samples were air quenched, but reduction treatments of n-type TCOs are common practices for increasing oxygen defects and therefore the conductivity and had not yet been performed. The room temperature conductivity of $Mg_xIn_{2-2x}Sn_xO_3$ before and after such a reduction procedure is shown in Figure 3 [27]. The conductivity of as-synthesized $Mg_xIn_{2-2x}Sn_xO_3$ was previously reported to be on the order of $10^0 \, \Omega \cdot cm$ (equivalent to 10^0 S/cm), but here, the conductivity of the as-synthesized $Mg_xIn_{2-2x}Sn_xO_3$ ranges from 5.8×10^1 S/cm^{-1} to 1.56×10^2 S/cm^{-1}, which are orders of magnitude greater. Furthermore, upon reduction, the conductivity of $Mg_xIn_{2-2x}Sn_xO_3$ can reach as high as 1064 S/cm, which makes that specific composition ($x = 0.05$) of potential interest as a commercial TCO material. Most notable is the severe drop in reduced conductivity from $x = 0.05$ to 0.1. Although conductivity typically decreases with decreasing In content in cosubstituted In_2O_3, a decrease of such magnitude is remarkable [11]. Powder XRD of the reduced samples do not exhibit any structural alterations, such as the emergence of secondary phases, that would account for the increased conductivity (relative to the pre-reduction conductivity).
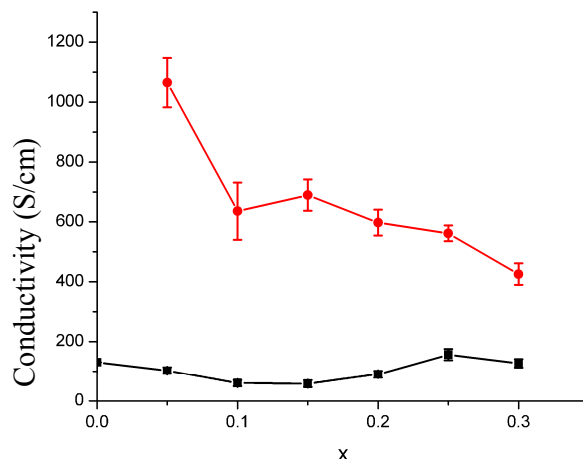
Figure 3. The conductivity of $Mg_xIn_{2-2x}Sn_xO_3$ before (squares) and after (circles) reduction. Error bars may be hidden by the data points. The point at $x = 0$ (pure In_2O_3) is reproduced from Reference [27], which follows a similar sample preparation.

With the favorable conductivity, the optical properties of the $Mg_xIn_{2-2x}Sn_xO_3$ solid solution are of interest and have also been assessed. Prior to reduction, pellets of $Mg_xIn_{2-2x}Sn_xO_3$ are pale yellow. After reduction, the same pellets are blue-gray. The optical band gaps of these materials are displayed in Figure 4 and, as can be observed, exhibit a ~0.1 eV increase upon reduction. Such an increase is common in n-type TCOs, as the reduction procedure increases the number of carriers, as evidenced by the increased conductivity, which enables a Burstein-Moss shift to occur, elevating the value of the optical band gap [28,29]. The fact that these materials are still n-type is confirmed by the Seebeck coefficients of the reduced samples (Figure S4), as they are negative. As mentioned in the discovery of the $Mg_xIn_{2-2x}Sn_xO_3$ system, the optical properties compare favorably with those of ITO. Thus the $Mg_xIn_{2-2x}Sn_xO_3$ solid solution can display both a high transparency and conductivity.

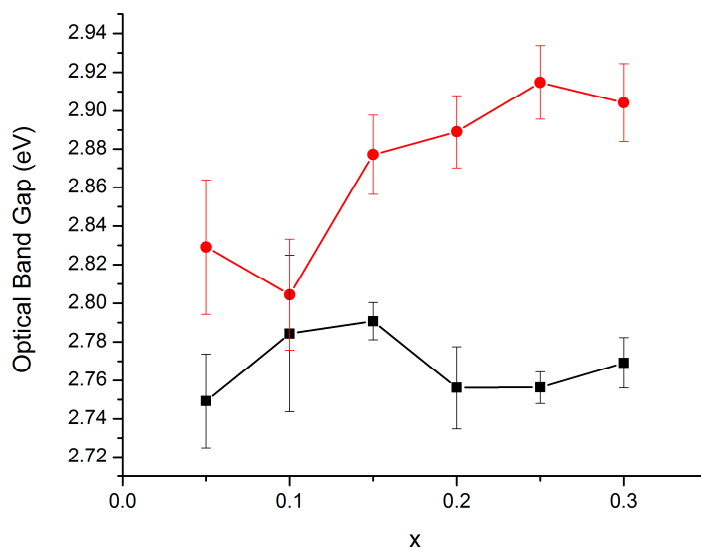**Figure 4.** Optical band gaps of the $Mg_xIn_{2-2x}Sn_xO_3$ solid solution before (squares) and after (circles) reduction.

3. Discussion

The greatest question facing a complete structural solution of the $Mg_xIn_{2-2x}Sn_xO_3$ system is the location(s) of the substituting elements. As demonstrated in Table 1, the joint Rietveld refinement

does not provide a definite occupancy of the structure. The structurally characterized members of the $M_xIn_{2-2x}Sn_xO_3$ (M = Ca, Ni, Cu, Zn, or Cd) family can be considered for guiding which of the aforementioned occupancy models is most accurate and the site occupancies of those that have been structurally characterized (M = Ni, Cu, Zn) are provided in Table 2. In all cases where Rietveld refinement of X-ray and neutron data were used, (1) a substantial amount of the M^{2+} substitute is present on the *d*-site; (2) there is some Sn^{4+} present on the *b*-site; and (3) the majority of M^{2+} is present on the site with the minority of Sn^{4+}. Unlike these overarching trends, relative site concentrations vary significantly, with a majority of M^{2+} being able to be present on either the *b*-site (M = Ni) or the *d*-site (M = Cu, Zn) and Sn^{4+} being entirely confined to the *b*-site (M = Cu) or nearly confined to the *d*-site (M = Ni). In the similar $In_{2-x}X_{2x/3}Sb_{x/3}O_3$ (X = Zn or Cu) system, however, Sb^{5+} only occupies the *b*-site, which is similar to the occupancy of Sn^{4+} in ITO and one of the best fits for $Mg_{0.1}In_{1.8}Sn_{0.1}O_3$ [9,10,30] With the similar goodness-of-fit parameters for the different occupancy models of $Mg_{0.1}In_{1.8}Sn_{0.1}O_3$, and the lack of a distinguishing trend in the $M_xIn_{2-2x}Sn_xO_3$ family, the most reliable conclusion from this structural investigation is that there must be some Mg on the *d*-site in $Mg_{0.1}In_{1.8}Sn_{0.1}O_3$.

Table 2. Site occupancies of reported cosubstituted bixbyite phases. Indium occupies the remaining site percentages.

Material	*M* Location (%)		Sn Location (%)		Method
	b-site	*d*-site	*b*-site	*d*-site	
$Cu_{0.275}In_{1.45}Sn_{0.275}O_3$	14	14	55	0	Rietveld Refinement—Neutron and X-ray [5]
$Ni_{0.5}InSn_{0.5}O_3$	65	11	2	33	Rietveld Refinement—Neutron and X-ray [5]
$Zn_{0.1}In_{1.8}Sn_{0.1}O_3$	No ordering, randomly distributed				Extended X-ray Absorption Fine Structure [14]
$Zn_{0.2}In_{1.6}Sn_{0.2}O_3$	No ordering, randomly distributed				Extended X-ray Absorption Fine Structure [14]
$Zn_{0.25}In_{1.5}Sn_{0.25}O_3$	18	11	50	0	Rietveld Refinement—Neutron and X-ray [5]
$Zn_{0.3}In_{1.4}Sn_{0.3}O_3$	No ordering, randomly distributed				Extended X-ray Absorption Fine Structure [14]
$Zn_{0.4}In_{1.2}Sn_{0.4}O_3$	No ordering, randomly distributed				Extended X-ray Absorption Fine Structure [14]

As shown in Table 2, the *M* = Zn system has been structurally characterized previously, but the reported occupancies are in conflict. Powder XRD studies suggest that Sn^{4+} only occupies the *b*-site, but additional studies with extended X-ray absorption fine structure (EXAFS) analysis have shown that both Zn and Sn are statistically distributed over the two available sites, with the probable formation of Sn clusters [5,14,15]. These contradicting results and the difficulty in definitively determining the site occupancies in $Mg_xIn_{2-2x}Sn_xO_3$, which is likely exacerbated by a microstructure disorder that results in the asymmetric peak shapes, suggest that an approach that avoids these difficulties is needed. Computational chemistry offers such a solution and the formation energies of different occupational models of $Zn_xIn_{2-2x}Sn_xO_3$ are calculated to seek a guiding principle and are provided in Figure 2b. Regardless as to the site occupancies, the higher the degree of separation, the lower the favorability of the formation, suggesting short range ordering may be present. The most favored points are when Zn and Sn are separated by 3.5769 Å, which translates to Zn and Sn being present in adjacent cation sites. Of the configurations that can have Zn and Sn adjacent, the mixed configurations, specifically when Zn is on the *d*-site and Sn is on the *b*-site, are most favored. These findings corroborate earlier reports of the stability of Zn on the *d*-site and Sn on the *b*-site. In the prior study, however, substitution on solely the *b*- or *d*-site was not mentioned [12]. This also fits with what is currently known experimentally, as Sn prefers the *b*-site in ITO and M^{2+} is always present on the *d*-site in $M_xIn_{2-2x}Sn_xO_3$. The inverse of these trends, when Sn is only present on the *d*-site and Zn is only present on the *b*-site are far less favored. Furthermore, the least favored configuration is when the *b*-site is not substituted, again suggesting that ITO's trends are still apparent in the cosubstituted systems. Interestingly, the stability switches to complete *b*-site substitution once the larger separations are considered. This suggests that local M^{2+}/Sn^{4+} interactions stabilize the structure, but the *b*-site is energetically favored if the interactions are negligible.

4. Materials and Methods

4.1. $Mg_xIn_{2-2x}Sn_xO_3$ Sample Preparation

Samples of $Mg_xIn_{2-2x}Sn_xO_3$ (x = 0.05, 0.1, 0.15, 0.2, 0.25, and 0.3) were prepared by mixing stoichiometric quantities of MgO, In_2O_3, and SnO_2 via a Fritsch planetary ball mill using agate media at 600 rpm for 4 cycles of 15 min, with pauses of 5 min between cycles. MgO was subjected to thermogravimetric analysis prior to this preparation and no carbonates or hydroxides were detected. Each sample was pressed into six, 13 mm in diameter cylindrical pellet under 16000 psi, buried in sacrificial powder in separate nested alumina crucibles, and heated to 1300 °C at a rate of 5 °C per min. The temperature was held at 1300 °C for 28 h before being cooled to 25 °C at a rate of 5 °C per min. Reduced samples were prepared on beds of sacrificial powder in alumina boats and ramped to 500 °C at a rate of 5 °C per min, dwelled at 500 °C for 7 h, and cooled to room temperature at a rate of 5 °C per min under a 5% hydrogen atmosphere (argon balance).

4.2. $Mg_xIn_{2-2x}Sn_xO_3$ Sample Characterization

Structure studies were performed with X-ray and neutron diffraction. A sample of $Mg_{0.1}In_{1.8}Sn_{0.1}O_3$ was prepared as a 2.54 cm cylindrical pellet and treated to the same procedure as above, but was not subjected to the reduction treatments. Instead, it was reground in the ball mill using tungsten carbide media at 600 rpm for 3 min and placed into a cylindrical (diameter = 6 mm) vanadium can and time-of-flight ND data were collected at the POWGEN beamline at the spallation neutron source at Oak Ridge National Laboratory. All data were collected at 26.85 °C with a central wavelength of 1.066 Å. Another portion of this sample was packed into a cylindrical Kapton capillary (inner diameter = 0.8 mm) and both ends were sealed with Q Compound (Apiezone). Synchrotron XRD data were collected at 11-BM on the advanced photon source at Argonne National Laboratory with a wavelength of 0.459 Å at 26.85 °C. Structural determinations used these data in joint Rietveld refinements via EXPGUI using GSAS [31,32]. One of the six pellets of each composition was removed after firing and a second pellet was removed after the reduction. Each pellet was ground in an agate mortar and pestle with ~10% silicon by mass, packed onto a flat glass slide, and subjected to Cu radiation in an Ultima IV (Rigaku, Tokyo, Japan) X-ray diffractometer. Scans were taken with 2θ beginning at 10 and ending at 70. The non-reduced patterns were the input used to calculate lattice parameters via whole pattern fitting (MDI Jade 2010). Silicon was used as an internal standard to correct for instrumental offset.

Conductivity studies were performed with a four-point probe. The sheet resistance of each pellet was measured after firing and reduction at five different locations on each face at room temperature using a four-point probe (Model 280PI, Four Dimensions, Inc. Hayward, CA, USA). Sample dimensions and masses were taken at each step to apply geometry and thickness corrections and the sheet resistance was converted to bulk conductivity [33]. Additionally, a porosity correction following the Bruggeman symmetric medium model was applied to each result, assuming that the air in the pellet acts as an insulating phase, following the same procedure as reported previously [13,34].

Band gaps were determined via diffuse reflectance. The diffuse reflectance of each pellet was measured from 250 to 800 nm at room temperature using a Lambda 1050 UV-Vis spectrophotometer with an integrating sphere attachment (PerkinElmer, Inc. Waltham, MA, USA) after firing and reduction. Background spectra were performed on compacted polytetrafluoroethylene. Optical band gaps were calculated by converting diffuse reflectance into Kubelka-Munk notation and approximating the optical band gap as the intersection of a linear extrapolation of the band edge and a linear extrapolation of the background [35–37].

Seebeck coefficients were measured on a Seebeck Measurement System (MMR Technologies, San Jose, CA, USA). Pre-and post-reduced samples were prepared as cylindrical pellets as described above. These were then cut down to ~1 mm × ~1 mm × ~5 mm rectangular prisms and mounted on an alumina stage with silver paste. Five measurements were taken every 15 °C between 305 K and 590 K.

4.3. $Zn_xIn_{2-2x}Sn_xO_3$ Computational Procedure

The structural energies and electronic properties were calculated using spin restricted DFT employed through the Vienna ab initio simulation package (VASP) [38–41]. Plane augmented wave (PAW) pseudopotentials were used with Perdew-Becke-Ernzerhof (PBE) exchange-correlation functionals [42]. A $2 \times 2 \times 2$ k-point grid and an energy cutoff of 400 eV were used in initial structural relaxations. The final grid was augmented (up to $5 \times 5 \times 5$) to guarantee adequate energy precision to distinguish between differing site configurations. Full 80 atom bixbyite unit cells were used, with varying amounts of pairwise zinc and tin substitution on the indium sites. To reduce computational costs, structural relaxations were mainly performed with tin and indium d-electrons in the pseudopotential core. Static calculations on relaxed cells were performed with indium d-electrons in the valence space to obtain possibly more accurate total energy values, and to assess possible effects on spectroscopic properties. Zinc d-states were always treated as valence, as the Zn d-band falls only a few eV below the Fermi energy. Although quantitative energies changed somewhat, energy ordering with respect to doping and ordering of structures was essentially unaltered. In retrospect, it was found that inclusion of the nominally fully occupied d^{10} shells of In, Sn and Zn in the valence space was useful in interpreting covalent contributions to bonding, and in elucidating subtle features of the optical densities of states.

5. Conclusions

In summary, we performed a thorough computational examination of $Zn_xIn_{2-2x}Sn_xO_3$ and an experimental examination of $Mg_xIn_{2-2x}Sn_xO_3$ to determine site preferences of the substituting atoms. In both instances, and the prior reported materials $M_xIn_{2-2x}Sn_xO_3$ (M = Ni, Cu, or Zn), a M^{2+} presence on the d-site of bixbyite and a Sn^{4+} presence on the b-site are suggested. Furthermore, the formation energies of $Zn_xIn_{2-2x}Sn_xO_3$ suggest a short range neighbor pairing of Zn and Sn. Property characterizations of $Mg_xIn_{2-2x}Sn_xO_3$ demonstrate that a reduction treatment makes its conductivity and optical properties much more competitive as a transparent conductor while continuing to be n-type despite the counterbalancing effect of Mg^{2+}.

Author Contributions: Karl Rickert, Nazmi Sedefoglu, Hamide Kavak, and Kenneth R. Poeppelmeier conceived and designed the experiments for $Mg_xIn_{2-2x}Sn_xO_3$. Jeremy Harris and Donald E. Ellis conceived and designed the experiments for $Zn_xIn_{2-2x}Sn_xO_3$. Karl Rickert, Jeremy Harris, and Nazmi Sedefoglu performed the experiments for their respective materials. Karl Rickert wrote the paper and analyzed the data.

References

1. Minami, T. Transparent conducting oxide semiconductors for transparent electrodes. *Semicond. Sci. Technol.* **2005**, *20*, S35–S44. [CrossRef]

2. Granqvist, C.G. Transparent conductors as solar energy materials: A panoramic review. *Sol. Energy Mater. Sol. Cells* **2007**, *91*, 1529–1598. [CrossRef]

3. Ginley, D.S.; Perkins, J.D. Transparent Conductors. In *Handbook of Transparent Conductors*; Ginley, D.S., Ed.; Springer: Boston, MA, USA, 2011; pp. 1–25.

4. Frank, G.; Kostlin, H. Electrical-properties and defect model of tin-doped indium oxide layers. *Appl. Phys. A* **1982**, *27*, 197–206. [CrossRef]

5. Bizo, L.; Choisnet, J.; Retoux, R.; Raveau, B. The great potential of coupled substitutions in In_2O_3 for the generation of bixbyite-type transparent conducting oxides, $In_{2-2x}M_xSn_xO_3$. *Solid State Commun.* **2005**, *136*, 163–168. [CrossRef]

6. Hoel, C.A.; Mason, T.O.; Gaillard, J.-F.; Poeppelmeier, K.R. Transparent conducting oxides in the ZnO-In_2O_3-SnO_2 system. *Chem. Mater.* **2010**, *22*, 3569–3579. [CrossRef]

7. Harvey, S.P.; Mason, T.O.; Buchholz, D.B.; Chang, R.P.H.; Korber, C.; Klein, A. Carrier generation and inherent off-stoichiometry in Zn, Sn codoped indium oxide (ZITO) bulk and thin-film specimens. *J. Am. Ceram. Soc.* **2008**, *91*, 467–472. [CrossRef]

8. Nomura, K.; Ujihira, Y.; Tanaka, S.; Matsumoto, K. Characterization and estimation of ito (indium-tin-oxide) by mossbauer spectrometry. *Hyperfine Interact.* **1988**, *42*, 1207–1210. [CrossRef]

9. Nadaud, N.; Lequeux, N.; Nanot, M.; Jové, J.; Roisnel, T. Structural studies of tin-doped indium oxide (ITO) and $In_4Sn_3O_{12}$. *J. Solid State Chem.* **1998**, *135*, 140–148. [CrossRef]

10. Mryasov, O.N.; Freeman, A.J. Electronic band structure of indium tin oxide and criteria for transparent conducting behavior. *Phys. Rev. B* **2001**, *64*, 233111. [CrossRef]

11. Palmer, G.B.; Poeppelmeier, K.R.; Mason, T.O. Conductivity and transparency of ZnO/SnO_2-cosubstituted In_2O_3. *Chem. Mater.* **1997**, *9*, 3121–3126. [CrossRef]

12. Lu, Y.-B.; Yang, T.L.; Ling, Z.C.; Cong, W.-Y.; Zhang, P.; Li, Y.H.; Xin, Y.Q. How does the multiple constituent affect the carrier generation and charge transport in multicomponent tcos of In-Zn-Sn oxide. *J. Mater. Chem. C* **2015**, *3*, 7727–7737. [CrossRef]

13. Rickert, K.; Sedefoglu, N.; Malo, S.; Caignaert, V.; Kavak, H.; Poeppelmeier, K.R. Structural, electrical, and optical properties of the tetragonal, fluorite-related $Zn_{0.456}In_{1.084}Ge_{0.460}O_3$. *Chem. Mater.* **2015**, *27*, 5072–5079. [CrossRef]

14. Proffit, D.E.; Buchholz, D.B.; Chang, R.P.H.; Bedzyk, M.J.; Mason, T.O.; Ma, Q. X-ray absorption spectroscopy study of the local structures of crystalline Zn-In-Sn oxide thin films. *J. Appl. Phys.* **2009**, *106*, 113524. [CrossRef]

15. Hoel, C.A.; Gaillard, J.F.; Poeppelmeier, K.R. Probing the local structure of crystalline ZITO: $In_{2-2x}Sn_xZn_xO_3$ ($x \leq 0.4$). *J. Solid State Chem.* **2010**, *183*, 761–768. [CrossRef]

16. Hoel, C.A.; Gallardo Amores, J.M.; Moran, E.; Angel Alario-Franco, M.; Gaillard, J.-F.; Poeppelmeier, K.R. High-pressure synthesis and local structure of corundum-type $In_{2-2x}M_xSn_xO_3$ ($x \leq 0.7$). *JACS* **2010**, *132*, 16479–16487.

17. Hoel, C.A.; Xie, S.; Benmore, C.; Malliakas, C.D.; Gaillard, J.-F.; Poeppelmeier, K.R. Evidence for tetrahedral zinc in amorphous $In_{2-2x}Zn_xSn_xO_3$ (a-ZITO). *Z. Anorg. Allg. Chem.* **2011**, *637*, 885–894. [CrossRef]

18. Hoel, C.A.; Buchholz, D.B.; Chang, R.P.H.; Poeppelmeier, K.R. Pulsed-laser deposition of heteroepitaxial corundum-type zito: Cor-$In_{2-2x}Zn_xSn_xO_3$. *Thin Solid Films* **2012**, *520*, 2938–2942. [CrossRef]

19. Proffit, D.E.; Philippe, T.; Emery, J.D.; Ma, Q.; Buchholz, B.D.; Voorhees, P.W.; Bedzyk, M.J.; Chang, R.P.H.; Mason, T.O. Thermal stability of amorphous Zn-In-Sn-O films. *J. Electroceram.* **2015**, *34*, 167–174. [CrossRef]

20. Ni, J.; Wang, L.; Yang, Y.; Yan, H.; Jin, S.; Marks, T.J.; Ireland, J.R.; Kannewurf, C.R. Charge transport and optical properties of mocvd-derived highly transparent and conductive Mg- and Sn-doped In_2O_3 thin films. *Inorg. Chem.* **2005**, *44*, 6071–6076. [CrossRef] [PubMed]

21. Vegard, L. The constitution of the mixed crystals and the filling of space of the atoms. *Z. Phys.* **1921**, *5*, 17–26. [CrossRef]

22. Shannon, R.D. Revised effective ionic-radii and systematic studies of interatomic distances in halides and chalcogenides. *Acta Crystallogr. Sect. A Found. Crystallogr.* **1976**, *32*, 751–767. [CrossRef]

23. Denton, A.R.; Ashcroft, N.W. Vegard law. *Phys. Rev. A* **1991**, *43*, 3161–3164. [CrossRef] [PubMed]

24. Haas, P.; Tran, F.; Blaha, P. Calculation of the lattice constant of solids with semilocal functionals. *Phys. Rev. B* **2009**, *79*, 085104. [CrossRef]

25. Sæterli, R.; Flage-Larsen, E.; Friis, J.; Løvvik, O.M.; Pacaud, J.; Marthinsen, K.; Holmestad, R. Experimental and theoretical study of electron density and structure factors in $CoSb_3$. *Ultramicroscopy* **2011**, *111*, 847–853. [CrossRef] [PubMed]

26. Hamilton, W.C. Significance tests on crystallographic r factor. *Acta Crystallogr.* **1965**, *18*, 502–510. [CrossRef]

27. Sunde, T.O.L.; Lindgren, M.; Mason, T.O.; Einarsrud, M.A.; Grande, T. Solid solubility of rare earth elements (Nd, Eu, Tb) in $In_{2-x}Sn_xO_3$—Effect on electrical conductivity and optical properties. *Dalton Trans.* **2014**, *43*, 9620–9632. [CrossRef] [PubMed]

28. Burstein, E. Anomalous optical absorption limit in InSb. *Phys. Rev.* **1954**, *93*, 632–633. [CrossRef]

29. Moss, T.S. The interpretation of the properties of indium antimonide. *Proc. Phys. Soc. Lond. Sect. B* **1954**, *67*, 775–782. [CrossRef]

30. Bizo, L.; Choisnet, J.; Raveau, B. Coupled substitutions in In_2O_3: New transparent conductors $In_{2-2x}M_{2x/3}Sb_{x/3}O_3$ (M = Cu, Zn). *Mater. Res. Bull.* **2006**, *41*, 2232–2237. [CrossRef]

31. Larson, A.C.; Von Dreele, R.B. *General structure analysis system (GSAS)*; Report LAUR; Los Alamos National Laboratory: Los Alamos, NM, USA; pp. 86–748.

32. Toby, B.H. 'Expgui', a graphical user interface for gsas. *J. Appl. Crystallogr.* **2001**, *34*, 210–213. [CrossRef]

33. Smits, F.M. Measurement of sheet resistivities with the 4-point probe. *Bell Syst. Tech. J.* **1958**, *37*, 711–718. [CrossRef]

34. McLachlan, D.S.; Blaszkiewicz, M.; Newnham, R.E. Electrical-resistivity of composites. *J. Am. Ceram. Soc.* **1990**, *73*, 2187–2203. [CrossRef]

35. Kubelka, P.; Munk, Z. An article on optics of paint layers. *Z. Tech. Phys.* **1931**, *12*, 593–603.

36. Wendlandt, W.W.; Hecht, H.G. *Reflectance Spectroscopy*; Interscience Publishers: New York, NY, USA, 1966.

37. Tandon, S.P.; Gupta, J.P. Measurement of forbidden energy gap of semiconductors by diffuse refectance technique. *Phys. Status Solidi* **1970**, *38*, 363. [CrossRef]

38. Kresse, G.; Hafner, J. Ab initio molecular-dynamics for liquid-metals. *Phys. Rev. B* **1993**, *47*, 558–561. [CrossRef]

39. Kresse, G.; Hafner, J. Ab-initio molecular-dynamics simulation of the liquid metal amorphous-semiconductor transition in germanium. *Phys. Rev. B* **1994**, *49*, 14251–14269. [CrossRef]

40. Kresse, G.; Furthmuller, J. Efficient iterative schemes for ab initio total-energy calculations using a plane-wave basis set. *Phys. Rev. B* **1996**, *54*, 11169–11186. [CrossRef]

41. Kresse, G.; Furthmuller, J. Efficiency of ab-initio total energy calculations for metals and semiconductors using a plane-wave basis set. *Comput. Mater. Sci.* **1996**, *6*, 15–50. [CrossRef]

42. Perdew, J.P.; Burke, K.; Ernzerhof, M. Generalized gradient approximation made simple. *Phys. Rev. Lett.* **1996**, *77*, 3865–3868. [CrossRef] [PubMed]